



CHALMERS
UNIVERSITY OF TECHNOLOGY

Entanglement of photonic modes from a continuously driven two-level system

Downloaded from: <https://research.chalmers.se>, 2025-05-12 02:55 UTC

Citation for the original published paper (version of record):

Yang, J., Strandberg, I., Vivas-Viaña, A. et al (2025). Entanglement of photonic modes from a continuously driven two-level system. *npj Quantum Information*, 11(1).
<http://dx.doi.org/10.1038/s41534-025-00995-1>

N.B. When citing this work, cite the original published paper.



Entanglement of photonic modes from a continuously driven two-level system



Jiaying Yang^{1,2}✉, Ingrid Strandberg¹, Alejandro Vivas-Viaña^{3,4}, Akshay Gaikwad¹, Claudia Castillo-Moreno¹, Anton Frisk Kockum¹, Muhammad Asad Ullah², Carlos Sánchez Muñoz^{3,4}, Axel Martin Eriksson¹ & Simone Gasparinetti¹✉

The ability to generate entangled states of light is a key primitive for quantum communication and distributed quantum computation. Continuously driven sources, including those based on spontaneous parametric downconversion, are usually probabilistic, whereas deterministic sources require accurate timing of the control fields. Here, we experimentally generate entangled photonic modes by continuously exciting a quantum emitter - a superconducting qubit - with a coherent drive, taking advantage of mode matching in the time and frequency domain. Using joint quantum state tomography and logarithmic negativity, we show that entanglement is generated between modes extracted from the two sidebands of the resonance fluorescence spectrum. Because the entangled photonic modes are perfectly orthogonal, they can be transferred into distinct quantum memories. Our approach can be utilized to distribute entanglement at a high rate in various physical platforms, with applications in waveguide quantum electrodynamics, distributed quantum computing, and quantum networks.

Entanglement is a fundamental property of quantum physics, describing nonlocal correlations that are paramount for secure quantum communications^{1–3}, remote quantum sensing^{4–6}, quantum algorithms^{7,8}, and large-scale distributed quantum computing^{9–11}. Traditionally, in quantum optics, entangled photons have been produced from spontaneous parametric downconversion in combination with beamsplitters and photodetectors for heralding^{12,13}. The probabilistic nature of this process can be inconvenient, and more recent experiments have been able to generate entangled photonic states on demand, i.e., deterministically, with emitted photonic quantum bits (qubits) defined either in the polarization^{14–16} or a time-bin^{17–19} degree of freedom.

The time-frequency degree of freedom can be a valuable tool for high-dimensional quantum information processing, and optical time- or frequency-bin entangled two-photon states are typically produced in parametric downconversion or spontaneous four-wave mixing processes^{20–23}. In these parametric processes, the temporal mode shape of the output is selected by the spectral shape of the pump²⁴. In the microwave frequency range, frequency-entangled states have been produced via Josephson junction circuit elements^{25–31}, but besides considering time-bin qubit encoding^{32,33}, the temporal degree of freedom has been overlooked.

Here, we demonstrate a simple scheme to generate entangled time-frequency bosonic states from the steady-state emission of a single quantum

emitter, a transmon-type superconducting circuit coupled to a waveguide. When the emitter is driven close to resonance, it exhibits resonance fluorescence^{34,35}, a cornerstone of quantum optics and a source of anti-bunched photons. Studies of frequency-filtered modes of the emission spectrum have unveiled a rich landscape of multi-photon processes, evidencing the generation of non-classical correlations^{36–41}. In the time domain, it has been predicted that under certain conditions, selected temporal modes from the resonance-fluorescence emission exhibit a negative Wigner function, a hallmark of nonclassicality^{42,43}, and this prediction has been experimentally verified⁴⁴.

In the present study, we combine the time and frequency dimensions by selecting two temporally overlapping, but spectrally orthogonal photonic modes. We provide evidence of entanglement through joint quantum state tomography of the two selected modes, from which we determine the logarithmic negativity as a measure of entanglement⁴⁵. For optimally chosen parameters, we show entanglement between the two modes with a logarithmic negativity of 0.062. The generated entangled photonic modes could be physically extracted and transferred to quantum memories to perform quantum information processing tasks, entanglement distribution, or entanglement distillation^{46–48}. The demonstrated method is agnostic to the physical platform and can be extended to consider emission from quantum systems with different level diagrams and pumping schemes. Our results

¹Department of Microtechnology and Nanoscience, Chalmers University of Technology, Göteborg, Sweden. ²Ericsson Research, Ericsson AB, Stockholm, Sweden.

³Departamento de Física Teórica de la Materia Condensada and Condensed Matter Physics Center (IFIMAC), Universidad Autónoma de Madrid, Madrid, Spain.

⁴Institute of Fundamental Physics IFF-CSIC, Madrid, Spain. ✉e-mail: jiyang@chalmers.se; simoneg@chalmers.se

thus open a new avenue to extract entanglement from continuously driven quantum systems.

Results

Implementation with a superconducting circuit

We utilize an X-mon-type⁴⁹ superconducting circuit capacitively coupled to a waveguide [Fig. 1(a)] as the quantum emitter. The transition frequency between the ground state and the first excited state of the emitter is $\omega_{ge}/2\pi = 4.94$ GHz. The relaxation rate of the emitter into the waveguide is $T/2\pi = 8$ MHz, corresponding to a relaxation time $T_1 = 1/T \sim 20$ ns. The waveguide connects to the input and output lines in a reflection configuration [Fig. 1(b)]. This setup guides the input field to the qubit via the input line and the waveguide. Subsequently, the reflected output field travels in the reverse direction through the waveguide, and we then measure it from the output line using a linear amplification chain (see Supplementary Material Sec. I for more details on the setup). In the experiment, we continuously drive the emitter and measure the propagating output field in the waveguide [Fig. 1(c)]. The drive has a strength characterized by the Rabi frequency Ω (see Supplementary Material Sec. IV for drive-strength calibration) and is on resonance with the fundamental transition of the emitter.

Defining the temporal modes

We apply two temporal filters $f_k(t)$ ($k = 1, 2$) to the output field, extracting single propagating modes \hat{a}_k out of the time-dependent output field $\hat{a}^{\text{out}}(t)$ as⁵⁰

$$\hat{a}_k = \int_{-\infty}^{\infty} dt f_k(t) \hat{a}^{\text{out}}(t), \quad (1)$$

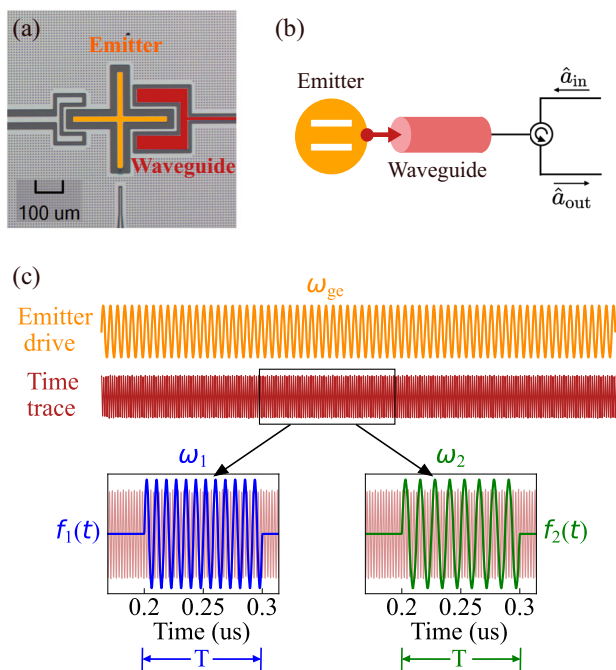


Fig. 1 | Experimental implementation for entangled-photon generation based on a superconducting circuit. **a** False-color optical micrograph of the device. A transmon qubit (orange) is capacitively coupled to a waveguide (red). The coupling element visible to the left of the transmon is not used in this work. **b** Schematic representation of the device and the measurement setup. \hat{a}_{in} and \hat{a}_{out} represent the input and output modes of the emitter’s field, respectively. **c** Temporal mode matching. The emitter is continuously driven at its frequency ω_{ge} (orange), and its emitted radiation is recorded as a time trace (red). The two insets represent the temporal filters $f_1(t)$ (blue) and $f_2(t)$ (green) applied on the time trace to match the two propagating modes.

The extracted modes fulfill bosonic commutation relations $[\hat{a}_k, \hat{a}_k^\dagger] = 1$, ensured by the normalization condition for the filter function $\int_{-\infty}^{\infty} dt |f_k(t)|^2 = 1$. Here, $\hat{a}_{\text{out}}(t)$ is given by the input-output relation^{50,51} $\hat{a}_{\text{out}}(t) = \sqrt{\Gamma} \hat{\sigma}(t) - \hat{a}_{\text{in}}(t)$, where $\hat{a}_{\text{in}}(t)$ is the input field.

Generally, it is possible to consider correlations between any pair of the propagating modes, including non-orthogonal ones. However, the orthogonality of the two temporal modes ensures that they are independent, and as such, can be physically extracted and mapped into separate quantum memories without added noise. For this reason, in the following, we will study correlations also for overlapping modes, but restrict to orthogonal modes when discussing entanglement (see Section “Two-mode entanglement” for more details). The condition for the two temporal filters to be orthogonal is

$$\int f_1^*(t) f_2(t) dt = 0. \quad (2)$$

where $f_1(t)$ and $f_2(t)$ are the two temporal filters with carrier frequencies ω_1 and ω_2 that fulfill

$$f_k(t) = v_k(t) \cdot e^{i(\omega_k t + \phi)}, \quad k = 1, 2. \quad (3)$$

Here, $v_k(t)$ denotes the wavepacket profile of the k th filter. We take both profiles to be identical boxcar functions of duration T , such that $v_1(t) = v_2(t) = v(t)$. For our case with two filters of the form Eq. (3), the orthogonality condition reduces to $(\omega_2 - \omega_1)/2\pi = m/T$, where m is an arbitrary integer. In this work, we use $T = 100$ ns, so the condition for orthogonality between the two modes is $(\omega_2 - \omega_1)/2\pi = m \cdot 10$ MHz. Additionally, modes that are separated by a large frequency detuning can also be considered orthogonal to a good extent.

To characterize the modes \hat{a}_k , we apply the corresponding filter functions to the measured time traces and collect enough statistics to calculate the relevant moments of the distribution. To characterize and remove the added noise from the amplification chain, we interleave measurements with the drive on and off, while maintaining the same settings for the temporal filters, and apply known techniques^{52,53} to deconvolve the probability distribution of the output field from the added noise. Additionally, the coherent background, originating from the reflected input, is removed during post-processing (see Methods “Removal of coherent background” for details). To justify this operation, we note that it can be physically implemented without significant degradation of the modes, for example, using a cancellation tone fed into the output via a directional coupler⁵⁴.

Optimization of parameters for a single mode

We first characterize the power emitted into a single mode, $f_1(t)$. We sweep the detuning $\Delta_1 = \omega_1 - \omega_{ge}$ between the modulation frequency of the temporal filter and the frequency of the emitter in the range of -40 MHz to 40 MHz, and measure the second-order moment $\langle \hat{a}_1^\dagger \hat{a}_1 \rangle$, the mean photon number (Fig. 2). With increasing drive power, side peaks appear at $\Delta_{\pm} \equiv \pm \Omega$ [Fig. 2(a)]. The frequency difference between the central peak and these side peaks corresponds to the drive Rabi frequency Ω . This observed structure is the well-known Mollow triplet^{35,55} of the resonance-fluorescence emission spectrum. In⁴¹, Lopez et al. theoretically propose a method for generating entangled photons by off-resonantly driving a two-level system and measuring the emission from the side peaks of the Mollow triplet. In contrast to the continuous mode analysis in⁴¹, in the rest of the paper, we focus on exploring the entanglement of temporally selected modes at the side-peak frequencies while coherently driving the qubit.

The duration of the filter affects its spectral content [Fig. 2(b)]; when the filter duration is short, the side peaks are not visible due to spectral broadening. We model our measurements with master equation and input-output theory (see Methods “Theoretical model”) and find a good agreement between theoretical predictions and experimental data.

In the following, we set the drive Rabi frequency to $\Omega = 4.04T$ and the duration of the temporal modes to $T = 100$ ns, corresponding to a well-developed Mollow triplet and a filter function for which the side peaks are

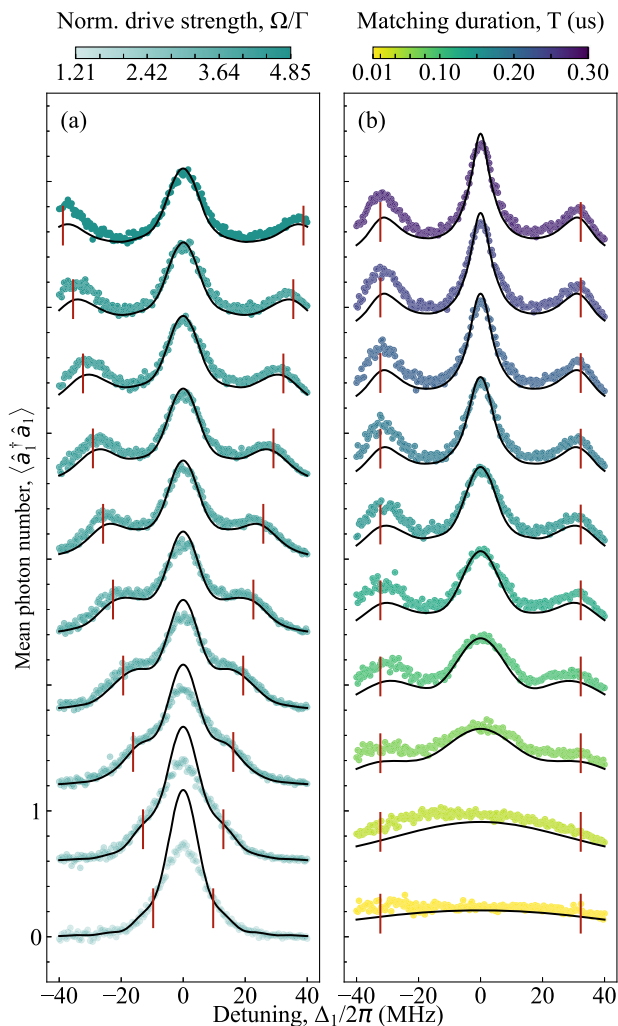


Fig. 2 | Second-order moment $\langle \hat{a}_1^\dagger \hat{a}_1 \rangle$ of a single propagating mode under varying drive conditions. **a** $\langle \hat{a}_1^\dagger \hat{a}_1 \rangle$ of the output mode as a function of Rabi frequency Ω , with the template-matching duration fixed at $T = 100$ ns. **b** $\langle \hat{a}_1^\dagger \hat{a}_1 \rangle$ as a function of template-matching duration T , with Ω fixed at 4.04Γ . In both panels, each curve is vertically offset by 0.6 for clarity. The filled circles are the measured data, while the black solid lines are the simulation results. The red vertical lines mark the positions of $\pm \Omega$, which match the location of the side peaks of the corresponding curves.

well resolved. This sideband-resolved regime allows us to obtain entanglement between the two orthogonal modes, as demonstrated in the next section.

Two-mode entanglement

We match the measured time trace with two simultaneously applied temporal filters, $f_1(t)$ and $f_2(t)$, to verify entanglement at optimal frequencies between the two selected propagating modes. The temporal profiles of the filters $v(t)$ are perfectly overlapping, $v_1(t) = v_2(t)$, while their frequencies, ω_1 and ω_2 , are independently varied in the range $[\omega_{ge} - 40$ MHz, $\omega_{ge} + 40$ MHz]. At each frequency of both temporal filters, we obtain the first- and second-order moments of the two propagating modes [See Fig. 3(a–h)]. The first row shows the simulated results (from the model in Methods “Theoretical model”) and the second row shows the measured results (See Methods “Moment denoising” to “Two-mode moments calculation” for data-analysis details). In the frequency regions around $(\Delta_1, \Delta_2) = (\Delta_-, \Delta_+)$ or (Δ_+, Δ_-) , near the anti-diagonal corners of the 2D maps, the moments $\langle \hat{a}_1 \rangle$ and $\langle \hat{a}_2 \rangle$ are close to zero [Fig. 3(a, b)], while the cross-second-order moment $\langle \hat{a}_1 \hat{a}_2 \rangle$ shows a peak [Fig. 3(g)]. This indicates a two-mode squeezing type of entanglement. While

in the region near $(\Delta_1, \Delta_2) = (\Delta_+, \Delta_+)$ or (Δ_-, Δ_-) , along the diagonal of the 2D moment maps, the cross-second-order moment $\langle \hat{a}_1^\dagger \hat{a}_2 \rangle$ shows a peak [Fig. 3(h)], indicating a beam-splitter type of entanglement. Note, however, that in this scenario, the two modes overlap both temporally and in frequency, and are generally not orthogonal. In the following, we focus on the frequency point (Δ_-, Δ_+) , where the two modes belong to opposite side peaks of the Mollow triplet and satisfy the frequency orthogonality condition in Eq. (2). At the selected point, we reduce the measurement noise level by performing more repetitions ($n = 2 \times 10^7$), allowing for the computation of moments up to the fourth order. Specifically, we compute moments $\langle (\hat{a}_1^\dagger)^{m_1} \hat{a}_1^{n_1} (\hat{a}_2^\dagger)^{m_2} \hat{a}_2^{n_2} \rangle$ for $m_1, n_1, m_2, n_2 \in \{0, 1, 2\}$ and $m_1 + n_1 + m_2 + n_2 \leq 4$, resulting in 27 moments excluding conjugation redundancy [Fig. 3(i, j)].

At this frequency point, we also reconstruct the density matrix of the two propagating modes by joint quantum state tomography [Fig. 4(a)]. The tomography utilizes least-squares optimization^{56,57} to find the most-likely density matrix corresponding to the measured moments [Fig. 4(a)]. In the reconstructed density matrix, multiple photon states are involved. Although the component $\langle 00|\rho|11 \rangle$ (where $|ij\rangle$ represents the number of photons in each mode) is the largest, there are additional off-diagonal elements (coherences) that are nonzero. The state overlap between the reconstructed and the simulated density matrices is 96.6%, with the state overlap defined as⁵⁸ $F(\rho, \rho') = \left(\text{Tr} \sqrt{\sqrt{\rho} \rho' \sqrt{\rho}} \right)^2$, where ρ and ρ' are the simulated and measured density matrices, respectively.

Further, to demonstrate that the two modes are entangled around the selected frequency point (Δ_-, Δ_+) , we perform joint quantum state tomography with $n = 2 \times 10^7$ repetitions across the frequency ranges $\Delta_1 \in [-40, -10]$ MHz and $\Delta_2 \in [10, 40]$ MHz. We then calculate the logarithmic negativity $E_{\mathcal{N}}$ from the reconstructed density matrices as a metric to quantify entanglement. We notice that the computation of $E_{\mathcal{N}}$ is very sensitive to small values of coherences of the density matrix. As a result, its value presents large fluctuations when we use least-squares optimization to reconstruct the density matrix. To reduce fluctuations in $E_{\mathcal{N}}$, we employ compressed-sensing optimization^{59,60}, which is a more aggressive approach that aims to find the optimal sparse solution of the density matrices. Given that our target density matrix is sufficiently sparse and we utilize a heavily reduced data set [using only 27 moments up to the fourth order, listed in Fig. 3(i, j), for reconstruction], compressed-sensing optimization effectively minimizes the impact of noisy coherent components in the reconstructed density matrices. This method thereby enables a clearer distribution of $E_{\mathcal{N}}$ [see Fig. 4(b), and see “Methods” “Joint Quantum state tomography” for details of the two optimization methods].

We observe the maximum $E_{\mathcal{N}}$ from the reconstruction near the frequency point (Δ_-, Δ_+) , with $E_{\mathcal{N}} = 0.128$, while that from the simulation reaches a maximum value of 0.062, at the same point [Fig. 4(c)] (See Supplementary Material Sec. II for simulations in more parameter regimes). We conjecture that the discrepancy between the simulated and measured $E_{\mathcal{N}}$ is due to our use of 27 moments up to fourth order, instead of the full 325 moments for a Fock-space cutoff at $N = 5$, which includes all cases fulfilling $m_1, n_1, m_2, n_2 \in \{0, 1, 2, 3, 4\}$. The excluded moments are between the fifth and 16th order, which are omitted due to high noise levels. Indeed, if we reconstruct the state using the same moments as done for the experiment, using simulated values, we obtain consistently higher values for $E_{\mathcal{N}}$, very close to the experiment [Fig. 4(d)]. By contrast, if we use all 325 combinations of simulated moments, we reproduce the $E_{\mathcal{N}}$ distribution obtained directly from the simulation (see direct comparison in Methods “Joint Quantum state tomography”). Based on these considerations, we conclude that the maximum $E_{\mathcal{N}}$ observed in our experiment is close to the simulation value of 0.062.

Discussion

Our work introduces and demonstrates an approach for generating entanglement in the time-frequency domain between propagating bosonic modes. Theoretical studies suggest that entangled photons are generated in the

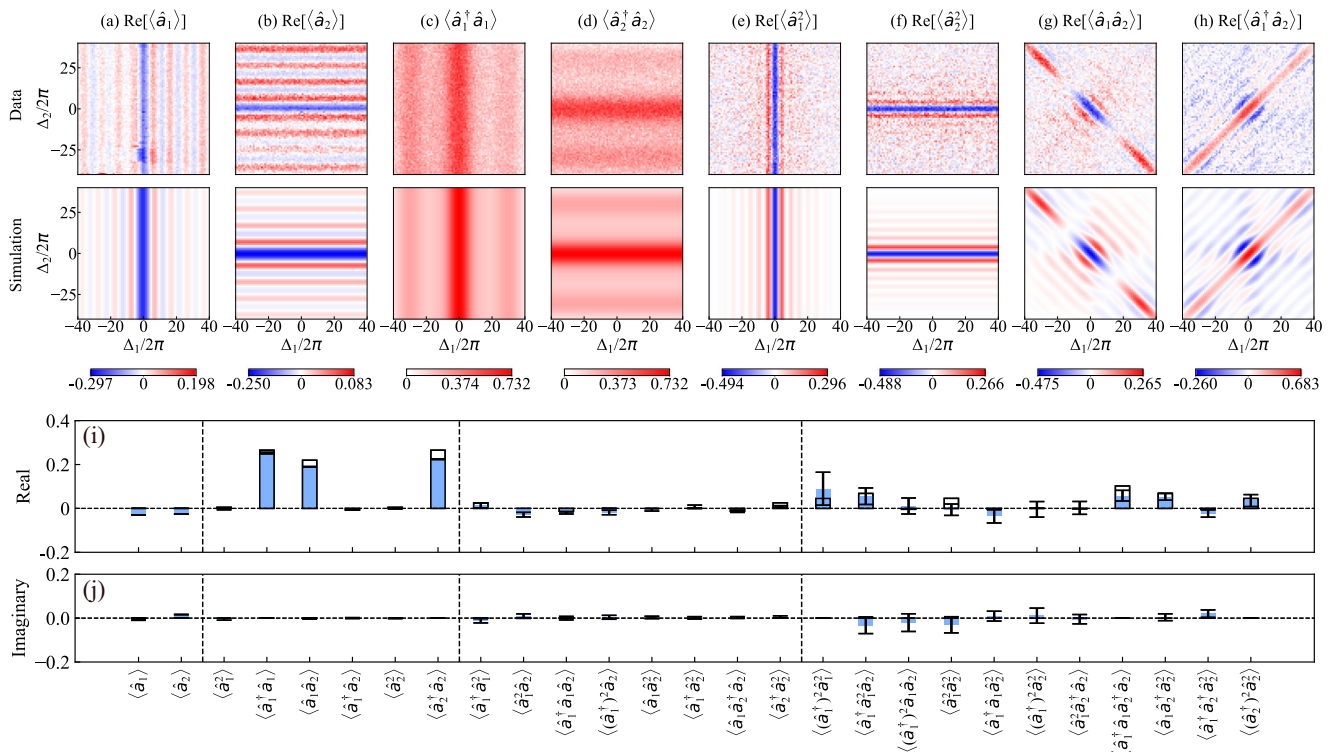


Fig. 3 | Moments and correlations of temporally matched modes. a–h Moments up to second order for the temporal modes defined in Eq. (3) as a function of frequency detunings $\Delta_k = \omega_k - \omega_{\text{ge}}$, where $k = 1, 2$. The upper row shows the data measured from the experiments. The lower row shows the 2D maps of the moments calculated from the simulation. The 2D map of the second-order moments $\langle\hat{a}_1^\dagger\hat{a}_1\rangle$ and $\langle\hat{a}_2^\dagger\hat{a}_2\rangle$ are normalized to have the same maximum value as

the simulation, and the other moments are scaled accordingly. **i, j** The real and imaginary parts of moments up to fourth order at the frequencies $(\Delta_1, \Delta_2) = (\Delta_-, \Delta_+)$. The blue bar is the measured data, while the black wireframe is the simulation. The error bar for each measured moment is obtained by splitting the data into 20 segments, calculating the moments for each segment, and obtaining the standard deviation over them.

Mollow triplet sideband emission observed in the resonance fluorescence from a single two-level emitter^{41,61}. We experimentally confirm generation of entanglement from steady-state resonance fluorescence in a continuously and coherently driven emitter by temporally matching two photonic modes from the continuous spectrum. At the frequencies of the opposite side peaks of the Mollow triplet, the reconstructed density matrix of the two-mode state exhibits a maximum logarithmic negativity of 0.128, which provides evidence of entanglement, aligning with our theoretical model of 0.062 after considering the limitations of our reconstruction scheme.

Entanglement in the time-frequency degree of freedom is a valuable asset for high-dimensional quantum information processing. In previous experiments, time-frequency modes have been utilized with entangled single-photon pairs^{24,62,63}. Our approach naturally incorporates multiphoton states, in which the number of photons is determined by the mode shape and output intensity of the quantum emitter. This experiment used a boxcar filter to define temporal modes, but simulation results presented in Supplementary Material II suggest that Hermite–Gauss modes yield higher logarithmic negativity. As such, there is potential to explore and optimize the mode shape to obtain states with higher entanglement or other desired properties.

While in our experiment we selected and characterized the modes simply by applying digital filters, these modes could be physically extracted and transferred to quantum memories^{64,65} to perform quantum information processing tasks or entanglement distribution. In the optical regime, the so-called quantum pulse gate⁶⁶ is capable of selecting an arbitrary time-frequency mode from a high-dimensional input^{24,67}. Selected modes can also be captured in cavities by tunable coupling^{68,69}, a technique which is well suited for microwave photons in superconducting circuits, in which cavities with adjustable couplers can be fabricated on-chip.

Compared to previous works^{17,27,70–73}, this system for entanglement generation has two main advantages: i) it uses a simple system with a single

emitter; ii) the entangled modes are generated by driving the emitter at steady state, so there is no timing constraint in applying the temporal filters. Additionally, the entanglement generation rate is only limited by the linewidth of the emitter, which can be made of the order of 1 GHz in superconducting circuits⁷⁴.

Although we focused on resonance fluorescence of a superconducting circuit, our method is broadly applicable since resonance fluorescence has been observed in a multitude of systems, including trapped ions^{75,76}, cold atoms⁷⁷, color centers in diamond^{78–80}, and semiconductor quantum dots^{81,82}, even at telecom wavelength^{83,84}. The method could also be applied using steady-state emission from other quantum systems as a resource, be it a comparatively simple arrangement such as a Kerr cavity⁸⁵, or more complex systems, for example, emitters in topological waveguides^{86–88} or those producing superradiance⁸⁹.

Methods

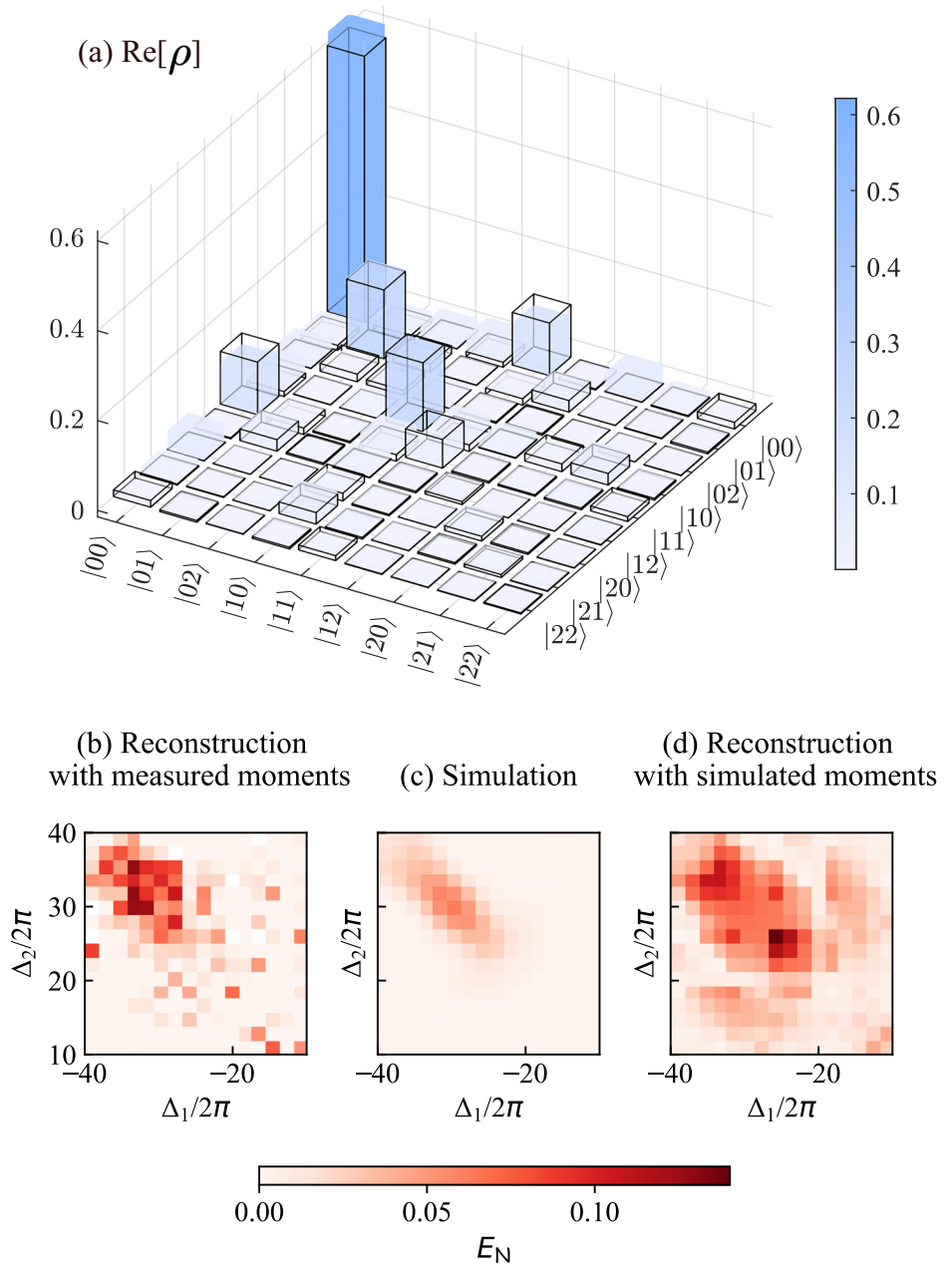
Theoretical model

Entanglement source. We describe the emitter as a two-level system, spanning a basis $\{|g\rangle, |e\rangle\}$, with transition frequency ω_{ge} and lowering operator $\hat{\sigma} = |g\rangle\langle e|$. We focus on the case of resonant driving, where the emitter is excited by a microwave pulse of frequency ω_{ge} and Rabi frequency Ω . In a frame rotating at the drive frequency and under a rotating-wave approximation, the Hamiltonian of the driven qubit is given by

$$\hat{H}_q = -i\Omega(\hat{\sigma}^\dagger - \hat{\sigma})/2. \quad (4)$$

The interaction between the qubit and the coplanar waveguide introduces incoherent processes by which the qubit is de-excited through spontaneous emission at a rate Γ . The dissipative dynamics of the reduced

Fig. 4 | Entangled temporal modes. Density matrix from the joint quantum state tomography and the obtained logarithmic negativity. **a** Comparing the real part of the reconstructed and simulated density matrices in Fock space up to $N = 5$, while only the selected lower-order components satisfying $N \leq 3$ are shown. The colored bars show the measurement result, and the black wireframes are the simulated prediction. The imaginary components of both the simulated and reconstructed density matrices, which are not shown, are less than 0.015 across all elements of the matrices. **b** The logarithmic negativity E_N reconstructed from the 27 measured moments over the frequency ranges $\Delta_1 \in [-40, -10]$ MHz and $\Delta_2 \in [10, 40]$ MHz. There are seven not-a-number points, shown in white, due to the optimizer failing to meet the standard deviation constraints of the moments at these frequency points during reconstruction. **c** The numerically simulated logarithmic negativity E_N over the same frequency range. **d** E_N reconstructed from the 27 simulated moments over the same frequency ranges. This distribution matches (c) if reconstructed using all combinations of simulated moments up to $N = 5$ (see “Methods”, “Joint Quantum state tomography”).



density matrix of the qubit is described by the master equation^{90–92}

$$d\hat{\rho}/dt = -i[\hat{H}_q, \hat{\rho}] + \frac{\Gamma}{2}\mathcal{D}[\hat{\sigma}]\hat{\rho}, \quad (5)$$

where we have defined the Lindblad superoperator as $\mathcal{D}[\hat{A}] \equiv 2\hat{A}\hat{\rho}\hat{A}^\dagger - \{\hat{A}^\dagger\hat{A}, \hat{\rho}\}$.

A diagonalization of \hat{H}_q yields two eigenstates $|\pm\rangle \equiv (|g\rangle \pm |e\rangle)/\sqrt{2}$ with corresponding eigenenergies $E_\pm = \pm \Omega$, which in the dressed-atom picture can be understood as hybrid light-matter states between the qubit and the drive. In the strong driving regime ($\Omega > \Gamma/4$), these eigenenergies can be resolved, and the emission spectrum of resonance fluorescence acquires the Mollow-triplet structure⁵⁵, with two side peaks emerging around a central peak at the drive frequency (see Fig. 2). This structure can be understood as transitions between the dressed eigenstates, the central peak at $\omega = \omega_{ge}$ corresponding to the doubly-degenerate transition $|\pm\rangle \rightarrow |\pm\rangle$, and the two side peaks at frequencies $\omega_\pm = \omega_{ge} \pm \Omega$ corresponding to transitions $|+\rangle \rightarrow |-\rangle$ and $|-\rangle \rightarrow |+\rangle$, respectively.

Joint quantum state of temporal modes. The density matrix describing the joint quantum states of both modes can be computed by using the input-output theory for quantum pulses^{93,94}. This approach treats the system and the emission as a cascaded quantum system⁵¹, in which the desired temporal mode is described as a virtual cavity (with annihilation operator \hat{a}_k) coupled non-reciprocally to the system with a time-dependent coupling. Here, we extend this approach to capture simultaneously several temporal modes by introducing two virtual cavities, resulting in the following cascaded master equation in the rotating frame of the drive:

$$\begin{aligned} \frac{d\hat{\rho}}{dt} = & -i[\hat{H}_q, \hat{\rho}] + \frac{\Gamma}{2}\mathcal{D}[\hat{\sigma}]\hat{\rho} + \sum_{k=1}^2 \frac{|g_k(t)|^2}{2} \mathcal{D}[\hat{a}_k]\hat{\rho} \\ & - \sum_{k=1}^2 \sqrt{\Gamma} \left(g_k^*(t)[\hat{a}_k^\dagger, \hat{\sigma}\hat{\rho}] + g_k(t)[\hat{\rho}\hat{\sigma}^\dagger, \hat{a}_k] \right). \end{aligned} \quad (6)$$

The temporal filters defined in Eq. (3) are encoded into time-dependent coupling^{95,96},

$$g_k(t) = -\frac{f_k(t)}{\sqrt{\int_0^t dt' |f_k(t')|^2}}. \quad (7)$$

In our implementation, the profile $v(t)$ of the temporal filters (see Eq. (3)) is defined as a normalized boxcar function $v(t) = \frac{1}{\sqrt{T}}[\Theta(t - t_0) - \Theta(t - t_0 - T)]$, with $\Theta(t)$ the Heaviside step function and t_0 the start time of the temporal filters. This results in the time-dependent couplings (in the rotating frame of the drive) $g_k(t) = -e^{i(\Delta_k t + \phi)} / \sqrt{t - t_0}$, where $\Delta_k \equiv \omega_k - \omega_{ge}$ is the k th sensor-laser detuning.

We note that related previous works^{41,97} used a version of the master equation in Eq. (6) that includes a factor $1/\sqrt{2}$ in the last term. Such a factor would stem from a description in which, prior to the capture of each mode, the output is physically split (e.g., by a beam splitter). In that description, the state obtained for each mode depends strongly on the total number of modes included, since the physical splitting has the effect of introducing important vacuum contributions. This would not accurately describe the digital filtering of the modes performed in this experiment, where the particular choice of f_1 should not affect the results obtained when filtering f_2 . This condition is not fulfilled by the cascaded multi-mode setups proposed in ref. 93. The master equation in Eq. (6), however, ensures independence of the filtered modes, and therefore serves as a good description of the type of mode-matching performed in this experiment.

Experimentally, $t_0 = 200$ ns is a sufficient waiting time to reach steady state. Numerically, we evolve the system until time $t_0 + T$ solving the time-dependent cascaded master equation Eq. (6) using QuTiP⁹⁸⁻¹⁰⁰. The simulated density matrix and moments of the two-mode state are obtained and used for comparison with experimental results. Then, we quantify the degree of entanglement between the two filtered temporal modes by means of the logarithmic negativity¹⁰¹⁻¹⁰³, a commonly used entanglement witness in bipartite systems. Given a general bipartite state, composed by systems A and B , the logarithmic negativity is defined as

$$E_{\mathcal{N}} \equiv \log_2(\|\rho^{T_A}\|_1), \quad (8)$$

where T_A denotes the partial transpose operation oversystem A , and $\|\cdot\|_1$ is the trace norm.

Moment denoising

Due to measurement noise arising from cable losses, amplification chain, mode-matching inefficiency, and other factors, the directly obtained total mode from temporal template matching, denoted as \hat{S}_k , does not solely represent the target modes \hat{a}_k^{out} . Instead, \hat{S}_k comprises both the target mode \hat{a}_k^{out} and an additional noise mode \hat{h}^\dagger , $\hat{S}_k = \hat{a}_k^{\text{out}} + \hat{h}^\dagger$. To remove the noise mode \hat{h}^\dagger , we operate an interleaved measurement to sweep between two cases with and without the qubit drive. In the first case, we measure the total mode, including both the targeted mode and the noise mode. In the second case, the target mode is left in vacuum and the measurement can be served as a reference of the noise mode. The switching between the two cases is repeated n times, with n varying from 10^5 to 2×10^7 across different measurements, given that the added noise photon from the amplification chain is $n_{\text{added}} = 11$ in our setup. We use number of repetitions $n = 10^5$ in Fig. 3(a-h), $n = 10^6$ in Fig. 2 and $n = 2 \times 10^7$ in Fig. 3(i, j) and Fig. 4. We then calculate the averaged moments from these repetitions. As we investigate higher-order moments, the number of required repetitions increases due to the escalating statistical errors associated with higher orders¹⁰⁴.

The first- and second-order moments of the two propagating modes¹⁰⁵, $\langle \hat{a}_k^{\text{out}} \rangle$ and $\langle (\hat{a}_k^{\text{out}})^\dagger \hat{a}_k^{\text{out}} \rangle$, are obtained by

$$\begin{aligned} \langle \hat{a}_k^{\text{out}} \rangle &= \langle \hat{S}_k - \hat{h}^\dagger \rangle, \\ \langle (\hat{a}_k^{\text{out}})^\dagger \hat{a}_k^{\text{out}} \rangle &= \langle \hat{S}_k^\dagger \hat{S}_k - \hat{S}_k^\dagger \hat{h} - \hat{S}_k^\dagger \hat{h}^\dagger + \hat{h} \hat{h}^\dagger \rangle, \end{aligned} \quad (9)$$

where the angle brackets represent the averaging over the n repetitions. These moments are with the coherent background from the reflected input drive; and in the next section, we discuss the subtraction of the coherent background.

Removal of coherent background

The relation between the input and the output modes is according to input-output theory¹⁰⁶

$$\sqrt{\Gamma} \hat{\sigma}_k^- = \hat{a}_k^{\text{out}} - \hat{a}_k^{\text{in}}. \quad (10)$$

The emission operator of the qubit, $\sqrt{\Gamma} \hat{\sigma}_k^-$, is the difference between the output field and the input field. In the main text, we choose to present experimental results and simulations for the emission operator of the qubit alone, that is, after the coherent input field has been removed. The subtraction of a coherent field of arbitrary amplitude and phase, corresponding to a displacement in phase space, is a physically justified operation. For example, in ref. 54, the subtraction is performed directly in the experimental setup, by adding a cancellation pulse through a weakly coupled directional coupler. Here, we remove the coherent background from the output mode obtained through measurement by post-processing instead.

We calculate the reflected input mode that is captured by the temporal filter through,

$$\langle \hat{a}_k^{\text{in}} \rangle = \Omega / \sqrt{\Gamma} \cdot \int_0^T e^{i(\omega_k t + \phi_B)} \cos(\omega_{\text{IF}} t) dt, \quad (11)$$

where Ω is the Rabi frequency of the drive signal, Γ is the decay rate of qubit to the waveguide, ω_k is the frequency of the temporal filter, and ω_{IF} is the down-converted frequency of the qubit.

Aside from the phase rotation parameters of the input mode, ϕ_B , we also introduce an amplification parameter A a phase rotation ϕ_A , to the measured output mode \hat{a}_k^{out} , and an amplification parameter B to the input mode \hat{a}_k^{in} . The same set of parameters A , B , ϕ_A , and ϕ_B is used for both modes. By optimally selecting these parameters, we aim to equate the simulated first-order moment with the transformed combination of these fields, thus achieving parameter identification and system characterization:

$$\langle \hat{a}_k \rangle_{\text{sim}} = \langle A e^{i\phi_A} \hat{a}_k^{\text{out}} - B \hat{a}_k^{\text{in}} \rangle. \quad (12)$$

Shifting our focus to the second-order moment, we relate simulation and measurement as follows:

$$\begin{aligned} \langle \hat{a}_k^\dagger \hat{a}_k \rangle_{\text{sim}} &= \langle (A e^{i\phi_A} \hat{a}_k^{\text{out}} - B \hat{a}_k^{\text{in}})^\dagger (A e^{i\phi_A} \hat{a}_k^{\text{out}} - B \hat{a}_k^{\text{in}}) \rangle \\ &= A^2 \langle (\hat{a}_k^{\text{out}})^\dagger \hat{a}_k^{\text{out}} \rangle + B^2 \langle (\hat{a}_k^{\text{in}})^\dagger \hat{a}_k^{\text{in}} \rangle \\ &\quad - AB \left(e^{-i\phi_A} \langle \hat{a}_k^{\text{in}} (\hat{a}_k^{\text{out}})^\dagger \rangle + e^{i\phi_A} \langle (\hat{a}_k^{\text{in}})^\dagger \hat{a}_k^{\text{out}} \rangle \right). \end{aligned} \quad (13)$$

By using a Scipy¹⁰⁷ optimizer to align the measured moments [calculated with Eq. (9)] with the simulated second-order moment according to Eq. (13), we find the optimal parameters A' , ϕ'_A , B' , and ϕ'_B . This procedure, including integration, optimization, and subtraction, is executed on both measured output modes. The optimal subtraction of the coherent background for each mode is

$$\sqrt{\Gamma} \langle \hat{\sigma}_k^- \rangle = A' e^{i\phi'_A} \langle \hat{a}_k^{\text{out}} \rangle - B' \langle \hat{a}_k^{\text{in}} \rangle. \quad (14)$$

This method identifies the emission operator, $\sqrt{\Gamma}\hat{\sigma}_k^-$, and ensures consistent normalization and phase rotation between the measured and simulated moments. For simplicity, we use $\hat{a}_k \equiv \sqrt{\Gamma}\hat{\sigma}_k^-$ to denote the modes without coherent background.

Two-mode moments calculation

After removing the coherent background from both propagating modes, we calculate the moments of the two propagating modes, \hat{a}_{k_2} , up to the fourth order. The recalculated moments $\langle (\hat{a}_1^\dagger)^{m_1} \hat{a}_1^{n_1} (\hat{a}_2^\dagger)^{m_2} \hat{a}_2^{n_2} \rangle$ satisfy $m_1, n_1, m_2, n_2 \in \{0, 1, 2\}$ and $m_1 + n_1 + m_2 + n_2 \leq 4$. These moments are computed as follows¹⁰⁵ in Eq. (15),

$$\begin{aligned} \langle (\hat{S}_1^\dagger)^{m_1} \hat{S}_1^{n_1} (\hat{S}_2^\dagger)^{m_2} \hat{S}_2^{n_2} \rangle &= \sum_{i_1, j_1, i_2, j_2=0}^{m_1, n_1, m_2, n_2} \binom{m_1}{i_1} \binom{n_1}{j_1} \binom{m_2}{i_2} \binom{n_2}{j_2} \\ &\times \langle (\hat{a}_1^\dagger)^{i_1} \hat{a}_1^{j_1} (\hat{a}_2^\dagger)^{i_2} \hat{a}_2^{j_2} \langle (\hat{h}_1^\dagger)^{m_1-i_1} \hat{h}_1^{n_1-j_1} (\hat{h}_2^\dagger)^{m_2-i_2} \hat{h}_2^{n_2-j_2} \rangle. \end{aligned} \quad (15)$$

All moments shown in Results have the coherent background removed through the procedure in Methods “Removal of coherent background” before the calculation.

Joint quantum state tomography

Optimization method. In the joint quantum state tomography of the two propagating modes, we reconstruct the optimal density matrix from the moments of the two modes using two different methods: least-squares optimization^{56,57} and compressed-sensing optimization^{59,60}. In this subsection, we discuss and compare the two methods.

Mathematically, the least-squares optimization method solves the following convex optimization problem to find the optimal density matrix ρ :

$$\min_{\rho} \left\| (\vec{B} - \mathcal{A}\vec{\rho}) \oslash \vec{\epsilon} \right\|_{\ell_2}, \quad (16a)$$

$$\text{subject to } \rho \geq 0, \quad (16b)$$

$$\text{Tr}(\rho) = 1, \quad (16c)$$

while the compressed-sensing optimization method is described by:

$$\min_{\rho} \|\vec{\rho}\|_{\ell_1}, \quad (17a)$$

$$\text{subject to } \left\| \vec{B} - \mathcal{A}\vec{\rho} \right\|_{\ell_2} \leq \|\vec{\epsilon}\|_{\ell_2}, \quad (17b)$$

$$\rho \geq 0, \quad (17c)$$

$$\text{Tr}(\rho) = 1, \quad (17d)$$

where $\vec{\rho}$ in the objective function given in Eq. (16a) and (17a) represents the vectorized form of the density matrix. In Eq. (16a) and (17b), \vec{B} is a column vector containing the experimentally measured or numerically simulated moments $\langle (\hat{a}_1^\dagger)^{m_1} \hat{a}_1^{n_1} (\hat{a}_2^\dagger)^{m_2} \hat{a}_2^{n_2} \rangle$. For both optimizations, the matrix \mathcal{A} is commonly referred to as the sensing matrix⁵⁷, which only depends on the operator basis set ($\{|i\rangle\langle j|\}$) and the measurement observable set ($\{(\hat{a}_1^\dagger)^{m_1} \hat{a}_1^{n_1} (\hat{a}_2^\dagger)^{m_2} \hat{a}_2^{n_2}\}$). $\vec{\epsilon}$ in Eq. (16a) and (17b) quantifies the level of uncertainty in the measurement, which is defined as the standard deviation vector. We calculate the standard deviation by splitting the data into 20 segments, computing moments for each segment, and then calculating the standard deviation across the moments from all segments. The Hadamard division operator \oslash represents the element-wise vector division in Eq. (16a). Furthermore, $\|\cdot\|_{\ell_1}$ and $\|\cdot\|_{\ell_2}$ represent the ℓ_1 and ℓ_2 norms, respectively. The ℓ_1 norm is calculated as the sum of the absolute values of the vector

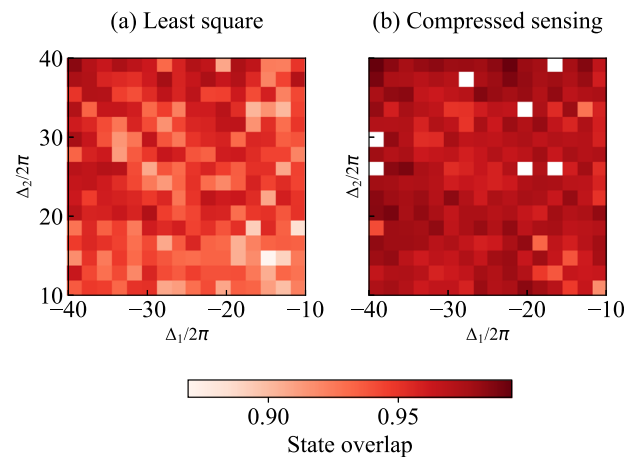


Fig. 5 | State overlap of the joint quantum state tomography. **a** State overlap between reconstructed density matrices (using 27 measured moments) and simulated density matrices, over the frequency ranges $\Delta_1 \in [-40, -10]$ MHz and $\Delta_2 \in [10, 40]$ MHz, utilizing least-squares optimization. **b** State overlap over the same frequency ranges, utilizing compressed-sensing optimization. Note the white points indicating not-a-number values due to optimization failures during reconstruction [see explanation under Fig. 4(b)].

components, while the ℓ_2 norm, also known as the Euclidean norm, is calculated as the square root of the sum of the squared vector components. The additional constraints given in Eq. (16b)–(16c) and Eq. (17c)–(17d) are positive semi-definite and unit trace conditions of the density matrix, ensuring its physical validity.

In the least-squares optimization, we minimize the least-squares distance between \vec{B} and $\mathcal{A}\vec{\rho}$ defined by ℓ_2 norm, weighting the different moments by dividing with $\vec{\epsilon}$ element-wisely [Eq. (16a)]. This approach assigns lower weights in the optimization cost function to moments with higher standard deviation and larger uncertainty, and higher weights to those with less uncertainty, thereby adjusting their influence in the optimization process accordingly. Least-squares optimization is a widely used method, which can find the optimal density matrix from the measured moments [Fig. 4(a)]. On the other hand, compressed-sensing optimization minimizes the ℓ_1 norm of $\vec{\rho}$ based on ρ being sparse—a property demonstrated in our simulation. This method is particularly advantageous when working with a heavily reduced dataset, such as the 27 moments used in our case. By emphasizing sparsity, compressed sensing effectively reconstructs the density matrix with fewer noisy coherent components, enabling us to see the distribution of logarithmic negativity $E_{\mathcal{N}}$ [Fig. 4(b)]. For both methods, we use convex optimization to find the minimization, using CVXPY¹⁰⁸.

Details on reconstructed density matrices. The state overlap between the reconstructed density matrix ρ' and the simulated density matrix is defined ρ as⁵⁸, $F(\rho, \rho') = \left(\text{Tr} \sqrt{\sqrt{\rho}\rho'\sqrt{\rho}} \right)^2$. Here we present the state overlap across the frequencies of the two photonic modes, for both optimizations (Fig. 5). We observe a higher state overlap when using compressed-sensing optimization, which results in a clearer representation of logarithmic negativity compared to other methods.

Furthermore, we calculate and present the purity of the density matrices at various frequencies of the two modes. The purity P of a density matrix ρ is defined as

$$P = \text{Tr}(\rho^2). \quad (18)$$

We illustrate the purity of the density matrices obtained from both experimental reconstructions and numerical simulations in Fig. 6.

Fig. 6 | Purity of density matrices. **a** Purity obtained from the reconstructed density matrices using 27 measured moments, utilizing least-squares optimization, over the frequency ranges $\Delta_1 \in [-40, -10]$ MHz and $\Delta_2 \in [10, 40]$ MHz. **b** Purity obtained from the same moments as in (a), but with compressed-sensing optimization. Note the white points indicating not-a-number values due to optimization failures during reconstruction [see explanation under Fig. 4(b)]. **c** Purity obtained from numerical simulations.

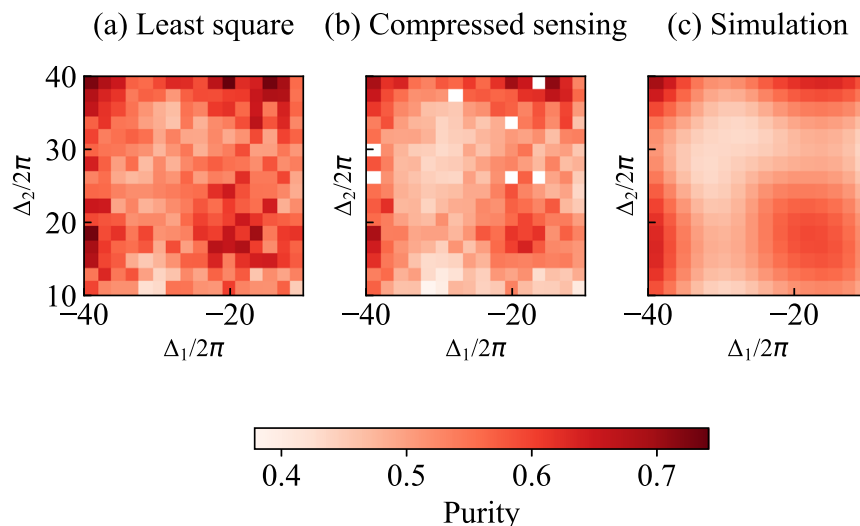
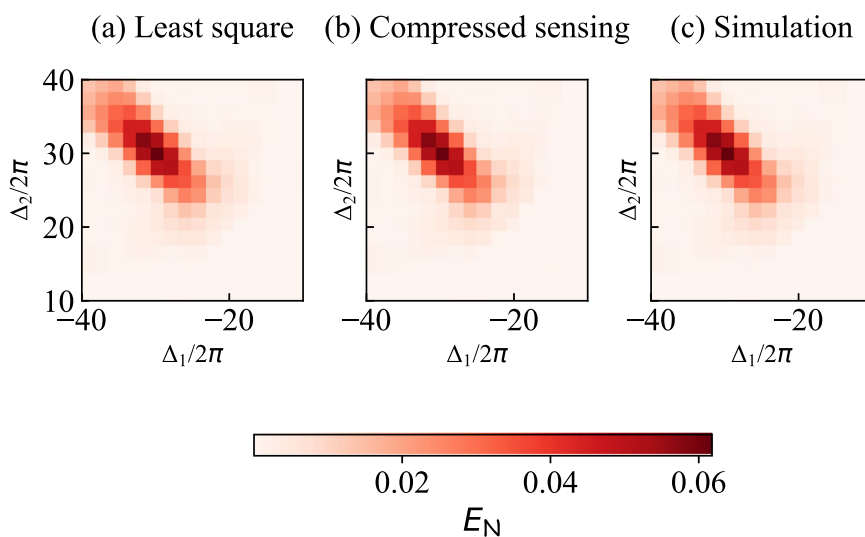


Fig. 7 | The logarithmic negativity E_N . **a** E_N reconstructed using all 325 simulated moments for a Fock space cutoff at $N = 5$, utilizing least-squares optimization, over the frequency ranges $\Delta_1 \in [-40, -10]$ MHz and $\Delta_2 \in [10, 40]$ MHz. **b** E_N reconstructed using the same simulated moments as in (a), but with compressed-sensing optimization, over the same frequency range. **c** E_N obtained from numerical simulation, over the same frequency range.



Reconstruction from the simulated moments. In Section “Two-mode entanglement”, we compare the logarithmic negativity E_N derived from the reconstructed density matrix using the measured moments with that obtained from simulated moments. Figure 3(c) presents E_N calculated from 27 moments with order up to four. Here, we extend this calculation to E_N obtain from reconstructed density matrices using all 325 noiseless simulated moments $((\hat{a}_1^\dagger)^{m_1} \hat{a}_1^{n_1} (\hat{a}_2^\dagger)^{m_2} \hat{a}_2^{n_2})$ for $m_1, m_2, n_1, n_2 \in \{0, 1, 2, 3, 4\}$ [Fig. 7(a) uses least-squares optimization and Fig. 7(b) uses compressed-sensing optimization], excluding conjugation redundancy. In both optimizations, we recover the same distribution as E_N obtained from the numerical simulation [Fig. 7(c)].

Data availability

Data is available from the corresponding author upon reasonable request.

Code availability

Code for analyzing data and generating plots is available from the corresponding author upon reasonable request.

Received: 12 August 2024; Accepted: 21 February 2025; Published online: 28 April 2025

References

1. Boström, K. & Felbinger, T. Deterministic secure direct communication using entanglement. *Phys. Rev. Lett.* **89**, 187902 (2002).
2. Lloyd, S. Power of entanglement in quantum communication. *Phys. Rev. Lett.* **90**, 167902 (2003).
3. Pennacchietti, M. et al. Oscillating photonic Bell state from a semiconductor quantum dot for quantum key distribution. *Commun. Phys.* **7**, 62 (2024).
4. Gottesman, D., Jennewein, T. & Croke, S. Longer-baseline telescopes using quantum repeaters. *Phys. Rev. Lett.* **109**, 070503 (2012).
5. Khabiboulline, E. T., Borregaard, J., De Greve, K. & Lukin, M. D. Quantum-assisted telescope arrays. *Phys. Rev. A* **100**, 022316 (2019).
6. Brown, M. R. et al. Interferometric imaging using shared quantum entanglement. *Phys. Rev. Lett.* **131**, 210801 (2023).
7. Jozsa, R. & Linden, N. On the role of entanglement in quantum-computational speed-up. *Proc. R. Soc. Lond. Ser. A: Math., Phys. Eng. Sci.* **459**, 2011–2032 (2003).
8. Nakhl, A. C., Quella, T. & Usman, M. Calibrating the role of entanglement in variational quantum circuits. *Phys. Rev. A* **109**, 032413 (2024).

9. Monroe, C. et al. Large-scale modular quantum-computer architecture with atomic memory and photonic interconnects. *Phys. Rev. A* **89**, 022317 (2014).
10. Daiss, S. et al. A quantum-logic gate between distant quantum-network modules. *Science* **371**, 614 (2021).
11. Akhtar, M. et al. A high-fidelity quantum matter-link between ion-trap microchip modules. *Nat. Commun.* **14**, 531 (2023).
12. Kwiat, P. G. et al. New high-intensity source of polarization-entangled photon pairs. *Phys. Rev. Lett.* **75**, 4337 (1995).
13. Ramelow, S. et al. Highly efficient heralding of entangled single photons. *Opt. Express* **21**, 6707 (2013).
14. Müller, M., Bounouar, S., Jöns, K. D., Glässl, M. & Michler, P. On-demand generation of indistinguishable polarization-entangled photon pairs. *Nat. Photonics* **8**, 224 (2014).
15. Istrati, D. et al. Sequential generation of linear cluster states from a single photon emitter. *Nat. Commun.* **11**, 5501 (2020).
16. Thomas, P., Ruscio, L., Morin, O. & Rempe, G. Efficient generation of entangled multiphoton graph states from a single atom. *Nature* **608**, 677 (2022).
17. Besse, J.-C. et al. Realizing a deterministic source of multipartite-entangled photonic qubits. *Nat. Commun.* **11**, 4877 (2020).
18. Knaut, C. M. et al. Entanglement of nanophotonic quantum memory nodes in a telecom network. *Nature* **629**, 573 (2024).
19. Ferreira, V. S., Kim, G., Butler, A., Pichler, H. & Painter, O. Deterministic generation of multidimensional photonic cluster states with a single quantum emitter. *Nat. Phys.* **20**, 865 (2024).
20. Olislager, L. et al. Frequency-bin entangled photons. *Phys. Rev. A* **82**, 013804 (2010).
21. Zhang, Z. et al. High-performance quantum entanglement generation via cascaded second-order nonlinear processes. *npj Quantum Inf.* **7**, 123 (2021).
22. Sabattoli, F. A. et al. A silicon source of frequency-bin entangled photons. *Opt. Lett.* **47**, 6201 (2022).
23. Clementi, M. et al. Programmable frequency-bin quantum states in a nano-engineered silicon device. *Nat. Commun.* **14**, 176 (2023).
24. Ansari, V., Donohue, J. M., Brecht, B. & Silberhorn, C. Tailoring nonlinear processes for quantum optics with pulsed temporal-mode encodings. *Optica* **5**, 534 (2018).
25. Eichler, C. et al. Observation of two-mode squeezing in the microwave frequency domain. *Phys. Rev. Lett.* **107**, 113601 (2011).
26. Schneider, B. H. et al. Observation of broadband entanglement in microwave radiation from a single time-varying boundary condition. *Phys. Rev. Lett.* **124**, 140503 (2020).
27. Gasparinetti, S. et al. Correlations and entanglement of microwave photons emitted in a cascade decay. *Phys. Rev. Lett.* **119**, 140504 (2017).
28. Peugeot, A. et al. Generating two continuous entangled microwave beams using a DC-biased Josephson junction. *Phys. Rev. X* **11**, 031008 (2021).
29. Esposito, M. et al. Observation of two-mode squeezing in a traveling wave parametric amplifier. *Phys. Rev. Lett.* **128**, 153603 (2022).
30. Perelshtein, M. R. et al. Broadband continuous-variable entanglement generation using a Kerr-free Josephson metamaterial. *Phys. Rev. Appl.* **18**, 024063 (2022).
31. Jolin, S. W. et al. Multipartite entanglement in a microwave frequency comb. *Phys. Rev. Lett.* **130**, 120601 (2023).
32. Kurpiers, P. et al. Quantum communication with time-bin encoded microwave photons. *Phys. Rev. Appl.* **12**, 044067 (2019).
33. Ilves, J. et al. On-demand generation and characterization of a microwave time-bin qubit. *npj Quantum Inf.* **6**, 34 (2020).
34. Kimble, H. & Mandel, L. Theory of resonance fluorescence. *Phys. Rev. A* **13**, 2123 (1976).
35. Astafiev, O. et al. Resonance fluorescence of a single artificial atom. *Science* **327**, 840 (2010).
36. Ulhaq, A. et al. Cascaded single-photon emission from the Mollow triplet sidebands of a quantum dot. *Nat. Photonics* **6**, 238 (2012).
37. Peiris, M. et al. Two-color photon correlations of the light scattered by a quantum dot. *Phys. Rev. B* **91**, 195125 (2015).
38. Peiris, M., Konthasinghe, K. & Muller, A. Franson interference generated by a two-level system. *Phys. Rev. Lett.* **118**, 030501 (2017).
39. López Carreño, J. C., Del Valle, E. & Laussy, F. P. Photon correlations from the mollow triplet. *Laser Photonics Rev.* **11**, 1700090 (2017).
40. Zubizarreta Casalengua, E., López Carreño, J. C., Laussy, F. P. & del Valle, E. Conventional and unconventional photon statistics. *Laser Photonics Rev.* **14**, 1900279 (2020).
41. López Carreño, J. C., Bermúdez Feijoo, S. & Stobińska, M. Entanglement in resonance fluorescence. *npj Nanophotonics* **1**, 3 (2024).
42. Strandberg, I., Lu, Y., Quijandría, F. & Johansson, G. Numerical study of Wigner negativity in one-dimensional steady-state resonance fluorescence. *Phys. Rev. A* **100**, 063808 (2019).
43. Quijandría, F., Strandberg, I. & Johansson, G. Steady-state generation of Wigner-negative states in one-dimensional resonance fluorescence. *Phys. Rev. Lett.* **121**, 263603 (2018).
44. Lu, Y. et al. Propagating Wigner-negative states generated from the steady-state emission of a superconducting qubit. *Phys. Rev. Lett.* **126**, 253602 (2021).
45. Plenio, M. B. Logarithmic negativity: a full entanglement monotone that is not convex. *Phys. Rev. Lett.* **95**, 090503 (2005).
46. Salari, V. et al. Cryogenic bridging via propagating microwave quantum teleportation. *AVS Quantum Sci.* **6**, 042001 (2024).
47. Zhang, H., Alsaedi, A., Hayat, T. & Deng, F.-G. Entanglement concentration and purification of two-mode squeezed microwave photons in circuit QED. *Ann. Phys.* **391**, 112 (2018).
48. Kurochkin, Y., Prasad, A. S. & Lvovsky, A. I. Distillation of the two-mode squeezed state. *Phys. Rev. Lett.* **112**, 070402 (2014).
49. Barends, R. et al. Coherent Josephson qubit suitable for scalable quantum integrated circuits. *Phys. Rev. Lett.* **111**, 080502 (2013).
50. Loudon, R. *The Quantum Theory of Light*, 3rd ed., Oxford Science Publications (Oxford University Press, Oxford, 2000).
51. Gardiner, C. W. and Zoller, P. *Quantum Noise: A Handbook of Markovian and Non-Markovian Quantum Stochastic Methods with Applications to Quantum Optics*, 3rd ed., Springer Series in Synergetics (Springer, 2004).
52. Eichler, C. et al. Experimental state tomography of itinerant single microwave photons. *Phys. Rev. Lett.* **106**, 220503 (2011).
53. Eichler, C., Bozyigit, D. & Wallraff, A. Characterizing quantum microwave radiation and its entanglement with superconducting qubits using linear detectors. *Phys. Rev. A* **86**, 032106 (2012).
54. Lu, Y. et al. Quantum efficiency, purity and stability of a tunable, narrowband microwave single-photon source. *npj Quantum Inf.* **7**, 140 (2021).
55. Mollow, B. R. Power spectrum of light scattered by two-level systems. *Phys. Rev.* **188**, 1969 (1969).
56. Nehra, R. et al. Generalized overlap quantum state tomography. *Phys. Rev. Res.* **2**, 042002 (2020).
57. Strandberg, I. Simple, reliable, and noise-resilient continuous-variable quantum state tomography with convex optimization. *Phys. Rev. Appl.* **18**, 044041 (2022).
58. Jozsa, R. Fidelity for mixed quantum states. *J. Mod. Opt.* **41**, 2315 (1994).
59. Shabani, A. et al. Efficient measurement of quantum dynamics via compressive sensing. *Phys. Rev. Lett.* **106**, 100401 (2011).
60. Rodionov, A. V. et al. Compressed sensing quantum process tomography for superconducting quantum gates. *Phys. Rev. B* **90**, 144504 (2014).

61. Sánchez Muñoz, C., Del Valle, E., Tejedor, C. & Laussy, F. P. Violation of classical inequalities by photon frequency filtering. *Phys. Rev. A* **90**, 052111 (2014).
62. Ashby, J. et al. Temporal mode transformations by sequential time and frequency phase modulation for applications in quantum information science. *Opt. Express* **28**, 38376 (2020).
63. Chiriano, F. et al. Hyper-entanglement between pulse modes and frequency bins. *Opt. Express* **31**, 35131 (2023).
64. Bao, Z. et al. On-demand storage and retrieval of microwave photons using a superconducting multiresonator quantum memory. *Phys. Rev. Lett.* **127**, 010503 (2021).
65. Matanin, A. R. et al. Toward highly efficient multimode superconducting quantum memory. *Phys. Rev. Appl.* **19**, 034011 (2023).
66. Eckstein, A., Brecht, B. & Silberhorn, C. A quantum pulse gate based on spectrally engineered sum frequency generation. *Opt. Express* **19**, 13770 (2011).
67. Harder, G., Ansari, V., Bartley, T. J., Brecht, B. & Silberhorn, C. Harnessing temporal modes for multi-photon quantum information processing based on integrated optics. *Philos. Trans. R. Soc. A* **375**, 20160244 (2017).
68. Xu, S., Shen, H. Z. & Yi, X. X. Demultiplexing of photonic temporal modes by a linear system. *Phys. Rev. A* **97**, 033841 (2018).
69. Yin, Y. et al. Catch and release of microwave photon states. *Phys. Rev. Lett.* **110**, 107001 (2013).
70. Wang, H. et al. Deterministic entanglement of photons in two superconducting microwave resonators. *Phys. Rev. Lett.* **106**, 060401 (2011).
71. Lang, C. et al. Correlations, indistinguishability and entanglement in Hong–Ou–Mandel experiments at microwave frequencies. *Nat. Phys.* **9**, 345 (2013).
72. Narla, A. et al. Robust concurrent remote entanglement between two superconducting qubits. *Phys. Rev. X* **6**, 031036 (2016).
73. Kannan, B. et al. Generating spatially entangled itinerant photons with waveguide quantum electrodynamics. *Sci. Adv.* **6**, eabb8780 (2020).
74. Forn-Díaz, P. et al. Ultrastrong coupling of a single artificial atom to an electromagnetic continuum in the nonperturbative regime. *Nat. Phys.* **13**, 39 (2017).
75. Cirac, J. I., Blatt, R., Parkins, A. S. & Zoller, P. Spectrum of resonance fluorescence from a single trapped ion. *Phys. Rev. A* **48**, 2169 (1993).
76. Bühner, V. & Tamm, C. Resonance fluorescence spectrum of a trapped ion undergoing quantum jumps. *Phys. Rev. A* **61**, 061801 (2000).
77. Bienert, M., Torres, J. M., Zippilli, S. & Morigi, G. Resonance fluorescence of a cold atom in a high-finesse resonator. *Phys. Rev. A* **76**, 013410 (2007).
78. Higbie, J. M. et al. Multiphoton-excited fluorescence of silicon-vacancy color centers in diamond. *Phys. Rev. Appl.* **7**, 054010 (2017).
79. Chen, D. et al. Quantum interference of resonance fluorescence from Germanium-vacancy color centers in diamond. *Nano Lett.* **22**, 6306 (2022).
80. Kumar, S. et al. Fluorescence enhancement of a single germanium vacancy center in a nanodiamond by a plasmonic Bragg cavity. *J. Chem. Phys.* **154**, 044303 (2021).
81. Muller, A. et al. Resonance fluorescence from a coherently driven semiconductor quantum dot in a cavity. *Phys. Rev. Lett.* **99**, 187402 (2007).
82. Makhonin, M. N. et al. Waveguide coupled resonance fluorescence from on-chip quantum emitter. *Nano Lett.* **14**, 6997 (2014).
83. Al-Khuzheyri, R. et al. Resonance fluorescence from a telecom-wavelength quantum dot. *Appl. Phys. Lett.* **109**, 163104 (2016).
84. Nawrath, C. et al. Resonance fluorescence of single In(Ga)As quantum dots emitting in the telecom C-band. *Appl. Phys. Lett.* **118**, 244002 (2021).
85. Strandberg, I., Johansson, G. & Quijandría, F. Wigner negativity in the steady-state output of a Kerr parametric oscillator. *Phys. Rev. Res.* **3**, 023041 (2021).
86. Mittal, S., Goldschmidt, E. A. & Hafezi, M. A topological source of quantum light. *Nature* **561**, 502 (2018).
87. Mehrabad, M. J. et al. Chiral topological photonics with an embedded quantum emitter. *Optica* **7**, 1690 (2020).
88. Vega, C., Porras, D. & González-Tudela, A. Topological multimode waveguide QED. *Phys. Rev. Res.* **5**, 023031 (2023).
89. Mlynek, J. A., Abdumalikov, A. A., Eichler, C. & Wallraff, A. Observation of Dicke superradiance for two artificial atoms in a cavity with high decay rate. *Nat. Commun.* **5**, 5186 (2014).
90. Breuer, H. P. and Petruccione, F. *The Theory of Open Quantum Systems* (Oxford University Press, 2007).
91. Carmichael, H. *An Open Systems Approach to Quantum Optics*, Lecture Notes in Physics Monographs, Vol. 18 (Springer Berlin Heidelberg, 1993).
92. García Ripoll, J. J. *Quantum Information and Quantum Optics with Superconducting Circuits*, 1st ed. (Cambridge University Press, 2022).
93. Kiilerich, A. H. & Mølmer, K. Input-output theory with quantum pulses. *Phys. Rev. Lett.* **123**, 123604 (2019).
94. Kiilerich, A. H. & Mølmer, K. Quantum interactions with pulses of radiation. *Phys. Rev. A* **102**, 023717 (2020).
95. Nurdin, H. I., James, M. R., and Yamamoto, N. Perfect single device absorber of arbitrary traveling single photon fields with a tunable coupling parameter: A QSDE approach, in *2016 IEEE 55th Conference on Decision and Control (CDC)* (IEEE, 2016) pp. 2513–2518.
96. Gough, J. E. & Zhang, G. Generating nonclassical quantum input field states with modulating filters. *EPJ Quantum Technol.* **2**, 15 (2015).
97. López Carreño, J. C., Del Valle, E. & Laussy, F. P. Frequency-resolved Monte Carlo. *Sci. Rep.* **8**, 6975 (2018).
98. Johansson, J., Nation, P. & Nori, F. QuTIP: An open-source Python framework for the dynamics of open quantum systems. *Comput. Phys. Commun.* **183**, 1760 (2012).
99. Johansson, J., Nation, P. & Nori, F. QuTIP 2: A Python framework for the dynamics of open quantum systems. *Comput. Phys. Commun.* **184**, 1234 (2013).
100. Lambert, N. et al. Qutip 5: The quantum toolbox in python, arXiv preprint arXiv:2412.04705 (2024).
101. Vidal, G. & Werner, R. F. Computable measure of entanglement. *Phys. Rev. A* **65**, 032314 (2002).
102. Plenio, M. & Virmani, S. An introduction to entanglement measures. *Quantum Inf. Comput.* **7**, 1 (2007).
103. Horodecki, R., Horodecki, P., Horodecki, M. & Horodecki, K. Quantum entanglement. *Rev. Mod. Phys.* **81**, 865 (2009).
104. da Silva, M. P., Bozyigit, D., Wallraff, A. & Blais, A. Schemes for the observation of photon correlation functions in circuit QED with linear detectors. *Phys. Rev. A* **82**, 043804 (2010).
105. Eichler, C. Doctoral Thesis, ETH Zurich (2013).
106. Gardiner, C. W. & Collett, M. J. Input and output in damped quantum systems: quantum stochastic differential equations and the master equation. *Phys. Rev. A* **31**, 3761 (1985).
107. Virtanen, P. et al. SciPy 1.0: fundamental algorithms for scientific computing in Python. *Nat. Methods* **17**, 261 (2020).
108. Diamond, S. & Boyd, S. CVXPY: a Python-embedded modeling language for convex optimization. *J. Mach. Learn. Res.* **17**, 2909 (2016).

Acknowledgements

The authors thank Janka Biznárová and Daniel Perez Lozano for help with fabrication, Kazi Rafsanjani Amin for technical assistance and useful discussions, Lars Jönsson for his help in making the sample holders, and

Giulia Ferrini for her input regarding the reviewer comments. The device in this work was fabricated in Myfab, Chalmers, a micro- and nano-fabrication laboratory. The traveling-wave parametric amplifier (TWPA) used in this experiment was provided by IARPA and Lincoln Labs. This work was supported by Ericsson Research and the Knut and Alice Wallenberg Foundation through the Wallenberg Centre for Quantum Technology (WACQT). S.G. acknowledges financial support from the European Research Council via Grant No. 101041744 ESQuAT. A.F.K. is also supported by the Swedish Research Council (grant number 2019-03696), the Swedish Foundation for Strategic Research (grant numbers FFL21-0279 and FUS21-0063), and the Horizon Europe programme HORIZON-CL4-2022-QUANTUM-01-SGA via the project 101113946 OpenSuperQPlus100. A.V.V. and C.S.M. acknowledge support from the Proyecto Sinérgico CAM 2020 Y2020/TCS- 6545 (NanoQuCo-CM), and MCINN projects PID2021-126964OB-I00 and TED2021-130552B-C21 and PID2021-127968NB-I00. C.S.M. also acknowledges the support of a fellowship from la Caixa Foundation (ID 100010434), from the European Union's Horizon 2020 Research and Innovation Programme under the Marie Skłodowska-Curie Grant Agreement No. 847648, with fellowship code LCF/BQ/PI20/11760026.

Author contributions

S.G. and C.S.M. planned the project. J.Y. performed the experiments and analyzed the data with input from A.M.E., I.S., S.G., and M.A.U. A.V.V., C.S.M., and I.S. built the theoretical model. J.Y. designed the device, and C.C.M. helped with the fabrication of the device. A.G. and A.F.K. operated the quantum state tomography. J.Y., I.S., and A.V.V. wrote the manuscript with feedback from all authors. S.G. and A.M.E. supervised this work.

Funding

Open access funding provided by Chalmers University of Technology.

Competing interests

The authors declare no competing interests.

Additional information

Supplementary information The online version contains supplementary material available at <https://doi.org/10.1038/s41534-025-00995-1>.

Correspondence and requests for materials should be addressed to Jiaying Yang or Simone Gasparinetti.

Reprints and permissions information is available at <http://www.nature.com/reprints>

Publisher's note Springer Nature remains neutral with regard to jurisdictional claims in published maps and institutional affiliations.

Open Access This article is licensed under a Creative Commons Attribution 4.0 International License, which permits use, sharing, adaptation, distribution and reproduction in any medium or format, as long as you give appropriate credit to the original author(s) and the source, provide a link to the Creative Commons licence, and indicate if changes were made. The images or other third party material in this article are included in the article's Creative Commons licence, unless indicated otherwise in a credit line to the material. If material is not included in the article's Creative Commons licence and your intended use is not permitted by statutory regulation or exceeds the permitted use, you will need to obtain permission directly from the copyright holder. To view a copy of this licence, visit <http://creativecommons.org/licenses/by/4.0/>.

© The Author(s) 2025